Journal Pre-proof

Role of orientation relationship for the formation of morphology and preferred orientation in NiAl-(Cr,Mo) during directional solidification

C. Schulz , A. Kauffmann , S. Laube , M. Kellner , B. Nestler , M. Heilmaier

Please cite this article as: C. Schulz , A. Kauffmann , S. Laube , M. Kellner , B. Nestler , M. Heilmaier , Role of orientation relationship for the formation of morphology and preferred orientation in NiAl-(Cr,Mo) during directional solidification, *Acta Materialia* (2022), doi: https://doi.org/10.1016/j.actamat.2022.117857

Role of orientation relationship for the formation of morphology and preferred orientation in NiAl-(Cr,Mo) during directional solidification
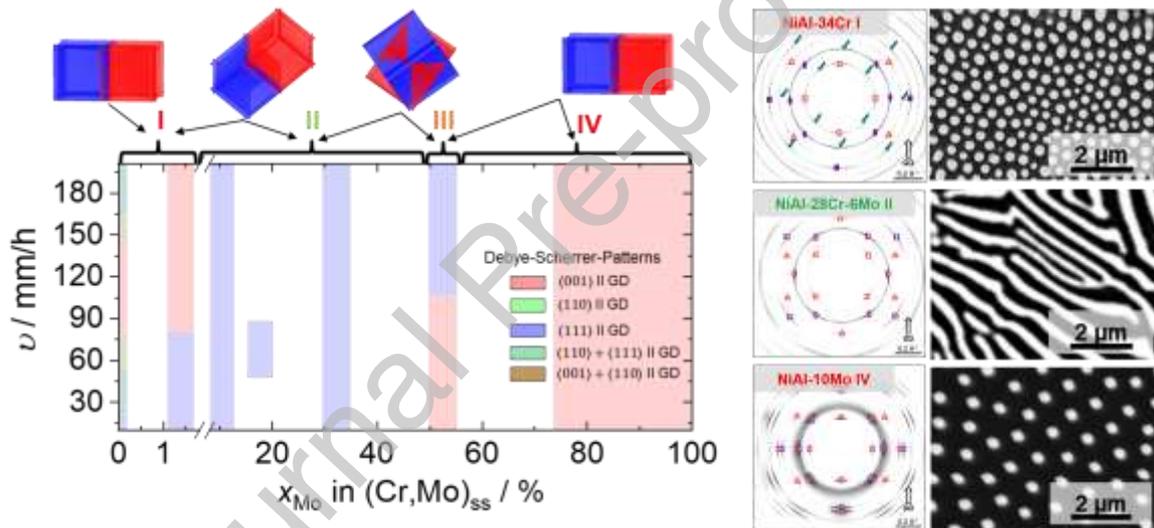
C. Schulz[a], A. Kauffmann[a]*, S. Laube[a], M. Kellner[a], B. Nestler[a] and M. Heilmaier[a]

[a] Institute for Applied Materials (IAM), Karlsruhe Institute of Technology (KIT), Engelbert-Arnold-Str. 4, 76131 Karlsruhe, Germany

*corresponding author
mail: alexander.kauffmann@kit.edu, phone: +4972160842346

Graphical Abstract

Abstract

In order to reveal the role orientation relationship for the formation of morphology and preferred orientation in directionally solidified NiAl-(Cr,Mo) eutectic alloys, a unique in-situ X-ray diffraction setup was utilized. Comprehensive analyses of the solidification front during processing demonstrate that the eutectic alloys crystallize with preferred crystallographic orientation of both phases with respect to the growth direction. These orientations of the eutectics prevail during growth of the fibrous or lamellar colonies and subsequent cooling as determined by ex-situ microstructural analysis. Depending on the composition and growth velocity, different preferred orientations were obtained resolving the ambiguity in literature regarding the reported components, e.g. strong ⟨001⟩ and ⟨111⟩ directions parallel to the growth direction but also additional minor ⟨110⟩ components. By the aid of in-situ experiments excluding the superimposed effect of different thermal expansion in comparison to previous experiments, a correlation between the evolving preferred orientation and lattice mismatch during solidification was found for alloys with low Mo content. Remarkably, *no* change in morphology between fibers and lamellae was associated to the transitions in preferred orientation. For larger Mo contents, two distinct orientation relationships between the A2 (Cr,Mo) solid solution and the B2 NiAl intermetallic phase were identified by ex-situ microstructural analysis, namely (1) cube-on-cube and (2) a 60° rotation about ⟨111⟩ in different colonies of one and the same sample. The morphology of these colonies were lamellar and fibrous, respectively. For the 60° relationship, the growth direction of both phase is unique, namely ⟨111⟩. Thus, morphology and preferred orientation are determined by the orientation relationship in this case.

Keywords: intermetallics, eutectics, in-situ directional solidification, orientation relationships, preferred orientation

1. Introduction

The B2 ordered intermetallic phase NiAl (CsCl prototype, space group Pm$\bar{3}$m, no. 221) has been considered for a long time as a promising candidate for high-temperature structural applications, due to its higher melting temperature (T_m = 1638 °C), lower density ($\rho \approx 6$ g/cm³) and excellent high-temperature oxidation resistance compared to Ni-based superalloys [1,2]. However, the monolithic intermetallic B2 phase suffers from low creep resistance and insufficient strength at elevated temperatures as well as from poor fracture toughness at room temperature [2,3]. Alloying NiAl with refractory metals such as Cr, Mo, Re, V and W can lead to quasi-binary NiAl-X eutectics with substantially improved mechanical properties [4–8]. The resulting eutectic microstructures are composed of a NiAl matrix and an embedded secondary fibrous or lamellar phase yielding a reinforcement [9–13]. Due to the small volume fraction of reinforcing phase in NiAl-Re and NiAl-W less improvement in the overall mechanical properties was achieved compared to NiAl-Cr, NiAl-Mo and NiAl-(Cr,Mo) [14]. However, NiAl-V with the highest volume fraction of reinforcing phase reveals only higher room temperature fracture toughness but less creep resistance compared to NiAl-(Cr,Mo) [8] presumably due to its lower liquidus temperature [14]. Hence, two-phase alloys from the NiAl-Cr-Mo eutectic system with the body centered cubic A2 (Cr,Mo) solid solution (W prototype, space group I m $\bar{3}$ m, no. 229) as strengthening phase are considered the most promising candidates for high-temperature applications. They possess a good combination of improved creep resistance at high temperatures as well as higher fracture toughness at room temperature compared to other NiAl-X eutectic alloys.

Several directionally solidified alloys have been studied in the past, namely NiAl-10Mo (unless stated otherwise, all concentrations are given in at.% in what follows) [4,5,8,15,16], NiAl-34Cr [4,8,11,17–19] and Cr-rich NiAl-(34-x)Cr-xMo with $0 \le x < 6$ at.% [4,8,20–23]. Although the existence of the eutectic trough connecting both pseudo-binary border systems was published in Ref. [24], the focus remained only on the above-mentioned alloys and mostly on their mechanical and oxidation properties [19,25–28]. The orientation relationship has either often been neglected or adopted from literature or cross-checked based on small investigated regions only [29,30]. Moreover, results on orientation relationship and preferred orientation of Refs. [5,31,32] were not pursued although the results appeared to be contradictory to the established studies of Refs. [4,17,33]. For instance, the additional orientation relationship (111)$_{NiAl}$ || (111)$_{Cr,Mo}$ and [$\bar{1}$10]$_{NiAl}$ || [01$\bar{1}$]$_{Cr,Mo}$, corresponding to a 60°

3

rotation about the [111] direction was reported in Ref. [31] for a Si- and Hf-doped NiAl-31Cr-3Mo alloy. The reported orientation relationship differs from the postulated cube-on-cube orientation relationship without further discussion. Ref. [5] reports a strong preferred orientation with ⟨001⟩ parallel to the growth direction and an additional ⟨111⟩ component developing in directionally solidified NiAl-34Cr, the latter of which is unexpected based on previous literature results. The study in Ref. [34] systematically investigated a series of alloys along the entire eutectic trough in the as-cast condition in terms of volume fraction and morphology of the reinforcing A2 (Cr,Mo) solid solution (abbreviated $(Cr,Mo)_{ss}$ in what follows) phase as well as orientation relationship with the matrix phase. Along the eutectic trough which is depicted in Fig. 1a, the evolving morphologies change from Cr-rich fibers (red region, **I**) to lamellae (green, **II**), adjacent a transit region with lamellae and fibers appears (orange, **III**) and finally, the morphology changes back to fibers, which are Mo-rich (red, **IV**) [34]. In order to provide an overview of the pseudo-binary border systems and the position of the eutectic trough, the entire system is depicted in Fig. 1b for reference.
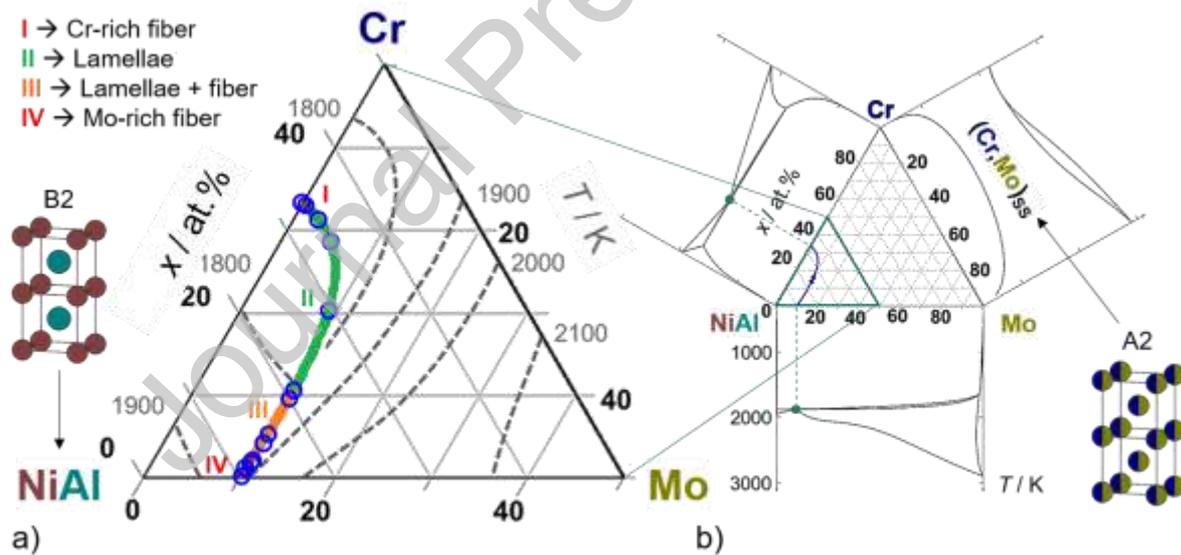

Fig. 1: a) Section of the liquidus projection of the NiAl-Cr-Mo system based on Ref. [25]. The color code refers to the classification according to the different morphologies in the as-cast condition made in Ref. [34]. Open blue symbols highlight the processed alloys. The crystal structures are B2 (CsCl prototype, space group Pm$\bar{3}$m, no. 221) and A2 (W prototype, space group I m $\bar{3}$ m, no. 229). b) Edge systems and liquidus projection in the NiAl-Cr-Mo-system based on work of Refs. [24,35]. a) is reproduced under the terms of the CC BY 4.0

4

Since the lattice parameter of the NiAl phase a_{NiAl} is almost constant and independent of the overall Mo and Cr concentration at room temperature, the lattice mismatch in the composite is predominantly controlled by the Mo concentration in $(\mathrm{Cr,Mo})_{ss}$ [34]. In-situ X-ray investigations during solidification demonstrated that alloys with intermediate Mo concentration are affected by segregation during rapid cooling due to their large solidification interval [34]. NiAl-9.6Cr-10.3Mo for example forms two solid solutions with significantly different lattice parameters $a_{(\mathrm{Cr,Mo})}$. In this alloy, also two different orientation relationships between $(\mathrm{Cr,Mo})_{ss}$ and NiAl were found: (1) a cube-on-cube relationship and (2) a relationship described by a rotation of 60° about the $\langle 111 \rangle$ axis [34]. Detailed investigations on the different colony types revealed, that the orientation of the selected nuclei is decisive rather than their subsequent growth [34]. The change in minimum interplanar spacing does not lead to a change in morphology, which emphasizes that the strains at the phase interface are less essential as the orientation of the selected nuclei [34]. Despite the previous investigations, the reason for the morphology change is still unclear. In order to assess the impact of the microstructure on the mechanical properties it is inevitable to understand the change in morphology but also the lattice mismatch evolution as well as formation of a preferred orientation.

The latter for instance is of interest when it comes to mechanical properties of the eutectics, since the NiAl matrix possess a mechanically "soft" ⟨111⟩ and "hard" ⟨001⟩ orientation [2].

By applying an in-situ directional solidification technique on various eutectic NiAl-(Cr, Mo) alloys, this paper addresses following objectives:

(i)   Resolving the ambiguity in literature regarding formation of ideal sites of preferred orientations during directional solidification and identifying its dependence on composition and growth rate.

(ii)   Revealing the fundamental reason for the formation of lamellar or fibrous morphology by highlighting its dependence on orientation relationship.

2.   Experimental

The elements Ni, Al, Cr and Mo of 99.97, 99.9, 99.96 and 99 % purity, respectively, were used to manufacture the desired eutectic compositions of NiAl-xCr-yMo (x = 34 … 0 at.%; y = 0 … 10.3 at.%) and binary NiAl. The alloys were synthesized by using an arc-melting device provided by Edmund Bühler GmbH (Germany). To ensure an oxygen-lean atmosphere, the chamber was evacuated multiple times and purged with Ar. Furthermore, a lump of Zr metal was melted prior to melting operations on NiAl-(Cr,Mo) in order to remove the residual oxygen in the chamber. To achieve sufficient homogeneity, the produced buttons were flipped and re-melted at least five times. Subsequently, the buttons were cast into a rod-shaped Cu mold. The rods were 12 mm and 170 mm in diameter and length, respectively. Since the overall mass loss was always lower than 0.3 wt.% and no specific loss of a certain element during arc-melting was noticed, the changes in alloy composition by evaporation are considered negligible. The nominal compositions of the investigated alloys are highlighted by blue open symbols in Fig. 1a. The sample designation in this paper is equivalent to these nominal compositions.

For directional solidification, a worldwide unique zone-melting device was used, which was described elsewhere [36] in very detail. This device was specifically designed for in-situ synchrotron directional solidification experiments at the High Energy Materials Science beamline (HEMS), PETRA III storage ring, Deutsches Elektronen-Synchrotron (DESY, Hamburg, Germany), operated by Helmholtz-Zentrum Hereon. During the process, the sample rotates about the rod axis and moves upward (lift) through the

induction coil that is used to heat up and locally melt the material, as shown in Fig. 3b. The rotation speed (R) was kept constant at 10 rpm and the growth velocity (v) varied from 18 to 180 mm/h. For the in-situ and ex-situ (subsequent to cooling to room temperature) experiments, a monochromatic beam at a photon energy of ~100 keV (wavelength of $\sim$ 0.124 Å) and a narrow cross section of $(1 \cdot 0.5)$ mm^2 was used for X-ray diffraction of the processing zone in transmission mode. A 2D PerkinElmer XRD 1621 solid-state detector of 2048 × 2048 pixels in size at pixel dimensions of 200 × 200 μm^2 (Massachusetts, USA) was placed perpendicular to the incident beam at a distance of $\sim$ 1.9 m. To calibrate the measurements, Si and CeO$_2$ powders were used as reference substances. A maximum 2θ angle of 6° with a step size of 0.006° was achieved [36]. The obtained synchrotron diffraction patterns during or subsequent to the directional solidification processes for various v were evaluated in terms of the evolving preferred crystallographic orientations. The different conditions of the process were: room temperature in the as-cast condition (as-cast, ex-situ), liquidus temperature (L, in-situ), a temperature just below the liquidus temperature to investigate the solidification front (SF, in-situ) where the first crystallites form and finally, room temperature in the directionally solidified condition (as-DS, ex-situ). The lattice parameter evolution of the individual phases was evaluated by analyzing the synchrotron diffraction patterns by means of azimuthal integration using the Fit2D software [37,38]. The resulting patterns were analyzed using the MAUD software [39,40] for Rietveld refinement and/or lattice parameter determination by the Nelson-Riley approach [41]. For the Rietveld refinement, known information about the materials (nominal composition, prototypes, compositions of the phases and phase fractions) and the instrument function (obtained on Si and CeO$_2$) were kept constant. Parameters for lattice dimension, polynomial background, domain size and lattice strain were refined. The results presented in Fig. 8 are exclusively analyzed by Rietveld refinement due to the overlapping peaks of B2 NiAl and A2 Cr. All other data presented in this article were obtained by applying both methods. Rietveld refinement and Nelson-Riley analyses yield consistent results of less than ±0.003 and ±0.001 Å for a_{NiAl} and $a_{\mathrm{(Cr,Mo)}}$, respectively. Some ex-situ synchrotron diffraction patterns obtained on NiAl-34Cr were quantitatively analyzed with respect to texture. The above mentioned materials parameters were kept constant while maximum ten parameters for harmonics were refined assuming axial symmetry with respect to the growth direction (GD, note the constant rotation speed R during operation) and a cube-on-cube orientation for the two phases (as independently verified).

For microstructural analysis, samples were cut by electro-discharge machining parallel and perpendicular to GD and were prepared by standard metallographic procedure using SiC grinding paper. Subsequent, polishing steps with diamond suspension down to 1 μm were performed. A final step utilizing a non-crystallizing oxide suspension was applied to remove the surface-near deformation layer. Scanning electron microscopy was performed using backscattered electron imaging (SEM-BSE) on a Zeiss EVO50 microscope by Carl Zeiss AG (Germany) at 20 kV and a spot size of 500. Additional orientation imaging microscopy by electron backscatter diffraction (EBSD) was carried out using an Auriga 60 dual-beam scanning electron and focused ion beam (FIB) microscope by Carl Zeiss AG (Germany) equipped with an EDAX (New Jersey, USA) Digiview EBSD camera. The scans were obtained at 20 kV with a step size of 200 nm and a field of view of 55×55 μm^2 using the TSL OIM Data Collection software. A2 (W prototype, space group I m $\overline{3}$ m, no. 229) was used for indexing of eight to twelve band centers. Image quality was used to differentiate the two phases. The TSL OIM Analysis software was used to analyze the acquired data.

3.   Results and discussion

For a better depiction, the presentation of the results is divided into different subsections according to important issues. First, the morphologies of directionally solidified alloys along the eutectic trough are presented in Sec. 3.1. The according preferred crystallographic orientations and orientation relationships between the phases in the entire temperature range between liquidus and room temperature are discussed in Sec. 3.2. Due to the simultaneous presence of mixed preferred orientation at intermediate growth velocity v = 60 mm/h, Sec. 3.3 deals with the influence of growth conditions on preferred orientation and microstructure formation in NiAl-34Cr. Furthermore, the evidence about the impact of lattice mismatch as the determining factor of preferred orientation is extended Mo-lean alloys. In Sec. 3.4, orientation relationship is proven to control morphology and preferred orientation in case of higher Mo contents.

3.1   Evolution of the as-DS microstructure along the eutectic trough

Fig. 2 displays the resulting microstructure parallel and perpendicular to GD for constant v = 60 mm/h. Microstructures representing the four characteristic regions in

Fig. 1a are visible in: Fig. 2a & b for alloys from region **I**, Fig. 2c corresponds to region **II**, Fig. 2d to region **III** and Fig. 2e & f to region **IV**, respectively. In all micrographs, dark contrast corresponds to the NiAl matrix and bright contrast to $(Cr,Mo)_{ss}$. An alignment of the microstructure parallel to GD was obtained at 60 mm/h for all alloys. For NiAl-9.6Cr-10.3Mo (**III**) however, the well-aligned regions were only of a few micrometers in length along GD (Fig. 2d). In comparison, the alloys close to the border systems, corresponding to regions **I** and **IV**, as well as those located in region **II** show pronounced alignment of the microstructural features along GD with little deviation.
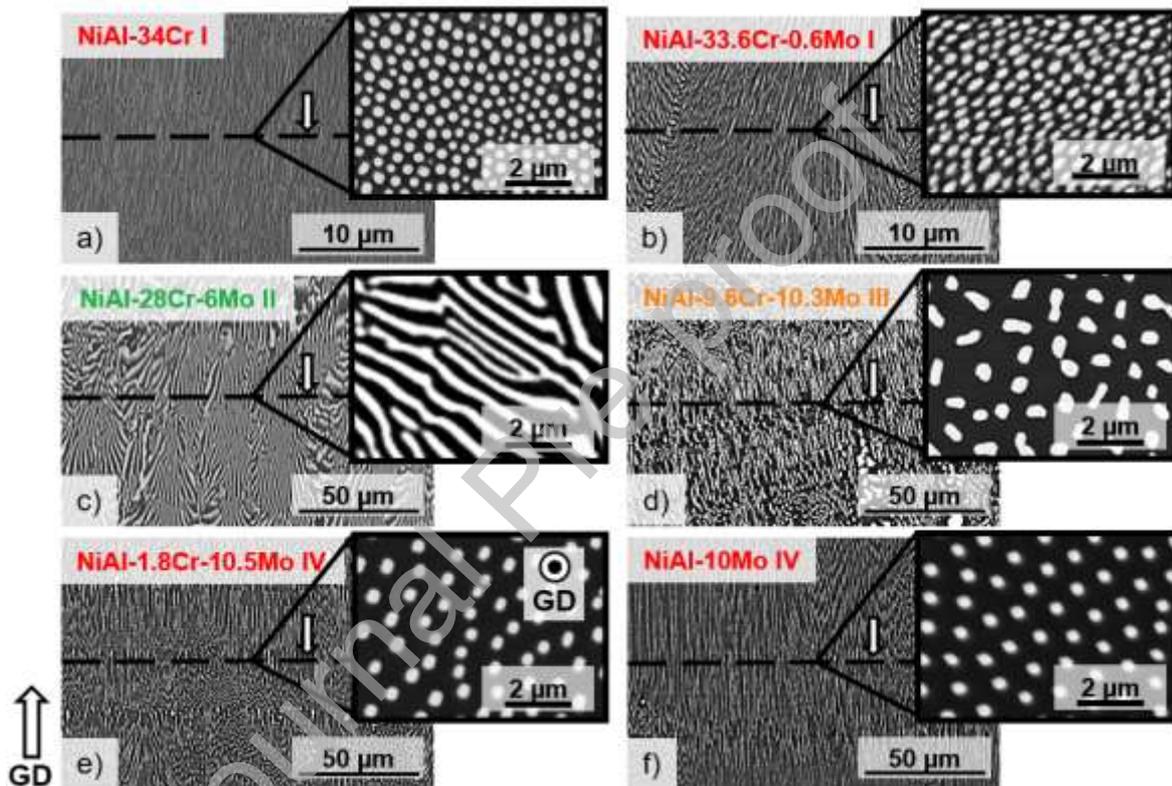

Fig. 2: Ex-situ SEM-BSE micrographs parallel (main images) and perpendicular (detailed views) to GD (indicated by arrow) subsequent to directional solidification at $v = 60$ mm/h: a) NiAl-34Cr, b) NiAl-33.4Cr-0.6Mo, c) NiAl-28Cr-6Mo, d) NiAl-9.6Cr-10.3Mo, e) NiAl-1.8Cr-10.54Mo and f) NiAl-10Mo. For a & b, a different magnification was chosen for the images parallel to GD as indicated by the changed scale bars. All other magnification are kept consistent.

The morphology of $(Cr,Mo)_{ss}$ is seen in the detailed micrographs perpendicular to GD. It is fibrous in regions **I** and **IV**, which was expected based on previous literature results. The morphology in region **II** is lamellar and also in accordance to literature. However, in the alloy from region **III** (NiAl-9.6Cr-10.3Mo in Fig. 2d), only fibrous $(Cr,Mo)_{ss}$ was observed in the well-aligned regions, although the same alloy showed a mixed

9

morphology in the as-cast condition not being subjected to directional solidification [34].

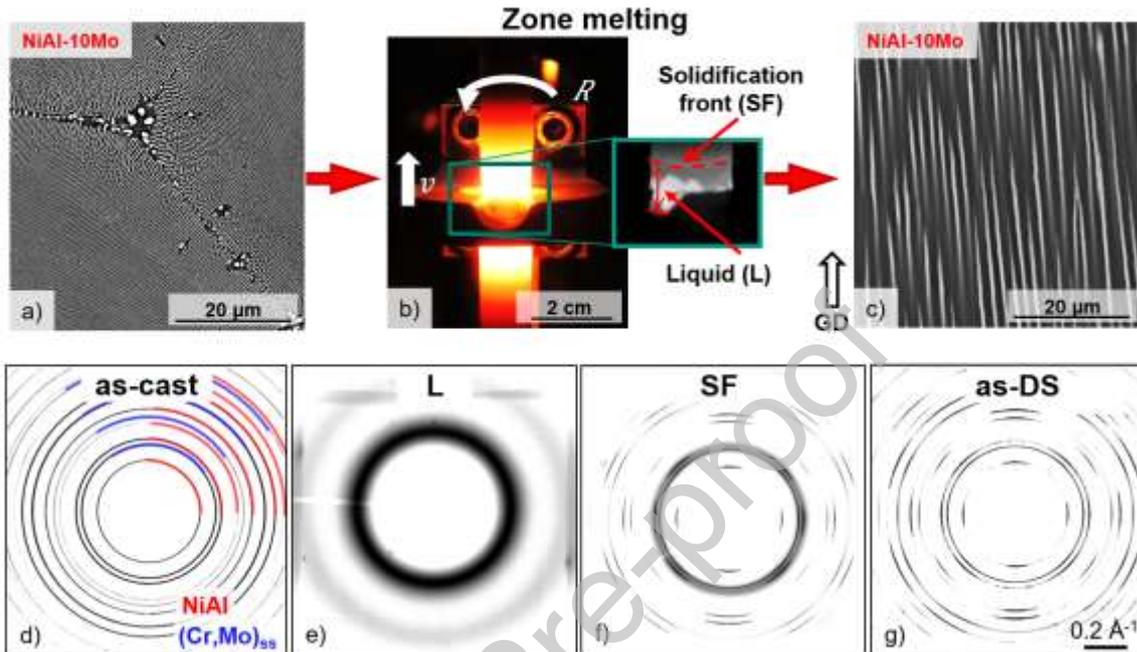## 3.2 In-situ investigation during directional solidification

Fig. 3: Ex-situ SEM-BSE micrographs of NiAl-10Mo in a) as-cast and c) as-DS condition. b) Photograph of the zone melting process during operation. Synchrotron diffraction patterns in d) as-cast condition (ex-situ) without preferred orientation, e) in the entire liquid state (L, in-situ), f) at the solidification front (SF, in-situ) and g) in as-DS condition (ex-situ) with preferred orientation. In d), the B2 NiAl rings are marked in red while blue rings correspond to the A2 $(Cr,Mo)_{ss}$.

In order to visualize the directional solidification process, Fig. 3 shows the microstructure at room temperature before (Fig. 3a) and subsequent to directional solidification (Fig. 3c). Additionally, the heating process and the formation of the liquid zone are displayed in Fig. 3b. The corresponding diffraction patterns are depicted in Fig. 3d to g. Fig. 3d represents the initial as-cast condition before directional solidification. Concentric rings with homogeneous intensity distribution are observed due to the random crystal orientation distribution of the colonies [42]. The diffraction rings belonging to the NiAl and $(Cr,Mo)_{ss}$ are marked in red and blue, respectively. Once the sample reaches the liquidus temperature, the long-range order disappears and the narrow rings of the crystalline phases vanish, while wide diffuse rings of the liquid appear (Fig. 3e). These rings have 2θ-angles of approximately 3.2° and 5.6° and are

10

related to typical diffraction angles based on mean interatomic distances in metallic liquids (determined to be approximately 2.14 Å and 1.22 Å, respectively) [43]. In Fig. 3f, both solid phases NiAl and $(Cr,Mo)_{ss}$ are observed besides the diffuse rings of the liquid when observing the solidification front. The intensity distribution along the rings is inhomogeneous for both phases, indicating the formation of a preferred orientation directly at the solidification front. Similar intensity distribution along the diffraction rings can be distinguished in Fig. 3g for the as-DS condition. Fig. 4 illustrates the intensity distributions in more detail. The patterns are formed by the superposition of the crystallographic arrangement of the phases in the sample coordinate system and the rotational symmetry about GD. The phases are aligned with ⟨001⟩ direction parallel to GD. Perpendicular to it, no preferred orientation exists. Hence, a complete fiber texture is present. The intensity maxima corresponding to the NiAl and $(Cr,Mo)_{ss}$ are assigned in red and blue, respectively (Fig. 4a). The sets of diffracting lattice planes are marked with symbols in Fig. 4b: square for {100} and {200}, oval for {110} and triangle for {111}. For instance, the normals of the $(001)_{NiAl}$, $(100)_{NiAl}$ and $(010)_{NiAl}$ planes are inclined by 0° and 90° with respect to GD and generate the intensity maxima on the innermost {100} diffraction ring (red square). In case of the {110} rings (oval symbols), the 90° inclination of (110) and $(1\bar{1}0)$ as well as the 45° inclination of the (101) and $(\bar{1}01)$ lead to the observed intensity variation for both phases. The normals of the $\{111\}_{NiAl}$ plane set are inclined by 54.7° with respect to GD and result in the intensity maxima highlighted by triangle symbols.
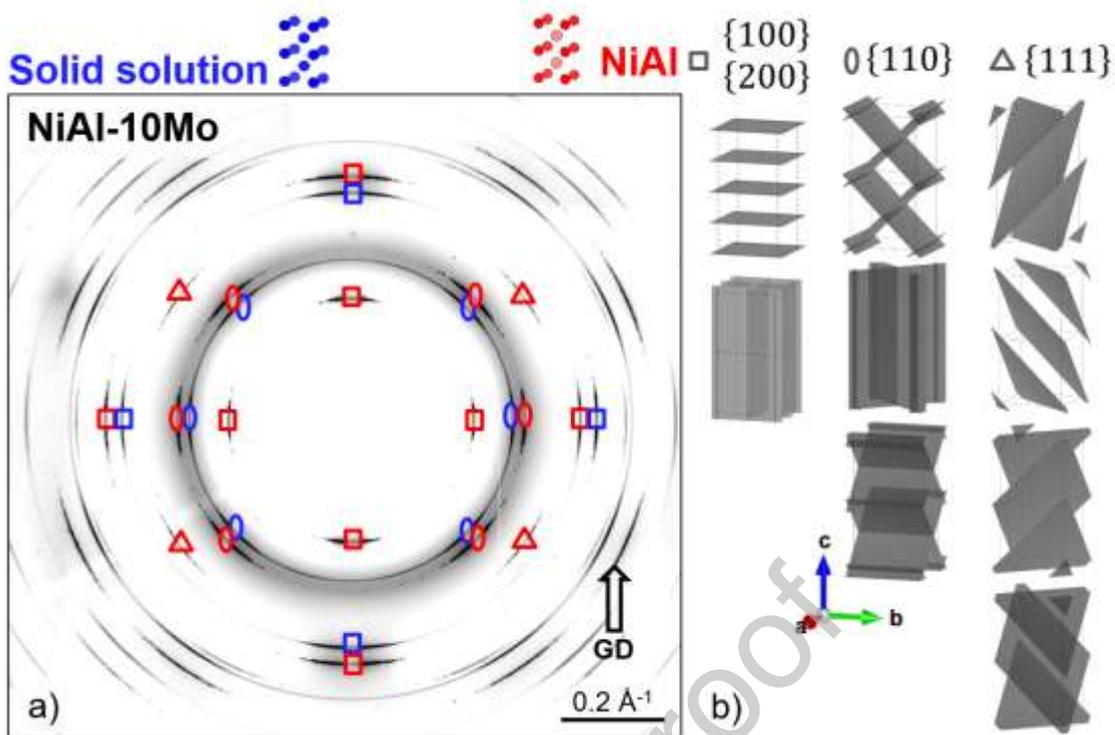
Fig. 4: a) In-situ synchrotron diffraction pattern of NiAl-10Mo taken at the SF. The intensity maxima on the A2 (Cr,Mo)$_{ss}$ rings are marked by blue symbols and those on the B2 NiAl rings by red symbols. The arrow indicates the GD. b) The sets of diffracting lattice planes are marked by symbols with their respective orientation to GD (consistently oriented to a)): square for {100} and {200}, oval for {110} and triangle for {111}.

As shown in our previous work [34], the orientation relationship in NiAl-10Mo is clearly cube-on-cube. As both phases have intensity maxima at the same positions along the rings, the cube-on-cube orientation relationship is also confirmed subsequent to directional solidification. Thus, (only) an alignment of both phases with ⟨001⟩ parallel to GD takes place during directional solidification compared to the as-cast condition. In the following, the synchrotron diffraction patterns of eutectic alloys at the SF and in as-DS condition are examined with respect to the occurrence of a preferred orientation upon directional solidification. The process parameters R and v were kept identical for all alloys discussed here.
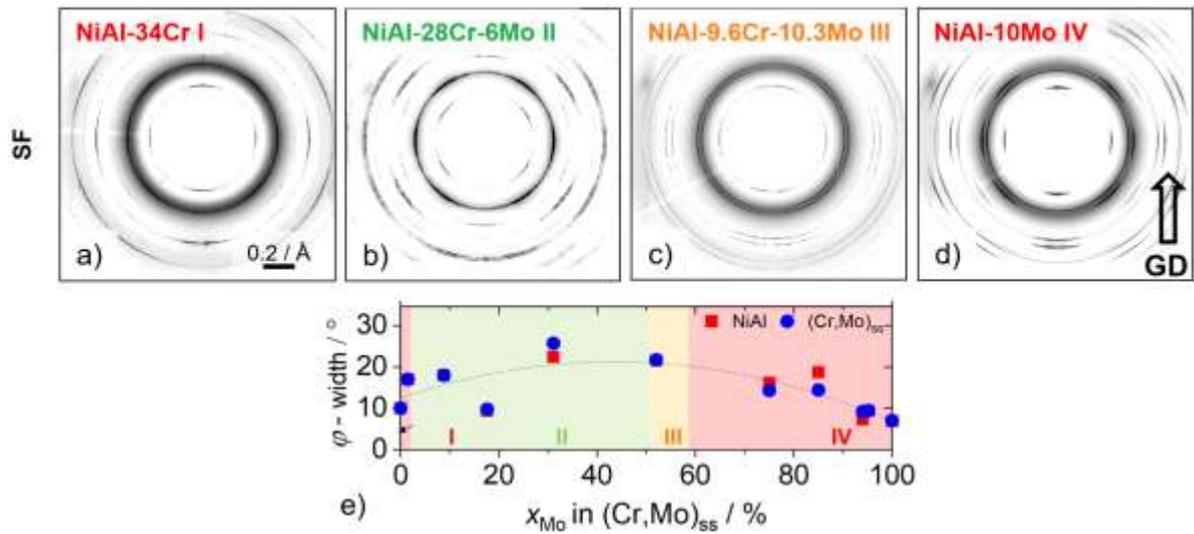
Fig. 5: In-situ synchrotron diffraction pattern at the SF: a) NiAl-34Cr, b) NiAl-28Cr-6Mo, c) NiAl-9.6Cr-10.3Mo and d) NiAl-10Mo. Growth velocity v was maintained at 60 mm/h for all alloys. The arrow indicates GD. GD is consistent for a) to d). Diffracting sets of lattice planes are indicated in Fig. 4a. e) Azimuthal angle φ widths of the intensity maxima as a function of Mo concentration in $(Cr,Mo)_{ss}$ (x_{Mo} in $(Cr,Mo)_{ss}$) obtained from a) to d). Red symbols and blue symbols represent the sharpness along the {200} diffraction rings of the B2 NiAl and A2 $(Cr,Mo)_{ss}$, respectively.

Apart from the homogenous, diffuse rings of the liquid, inhomogeneous intensity distributions along the rings of the two solid phases were observed for all alloys (Fig. 5a to d), which allows the conclusion that all eutectic NiAl-(Cr,Mo) alloys tend to crystallize with preferred orientation. The intensity variation along the rings in Fig. 5a, c & d indicates a ⟨001⟩ direction parallel to GD in the regions **I**, **III** and **IV**, respectively. In region **II** (Fig. 5b), the intensity distribution indicates a ⟨111⟩ parallel to GD. The deviation from the ideal preferred orientation changes along the eutectic trough as indicated by the varying intensity concentration along the diffraction rings. Manually determined φ widths of the intensity maxima along the {200} diffraction rings are plotted as a function of composition (x_{Mo} in $(Cr,Mo)_{ss}$) in Fig. 5e to quantify the changes. These rings where chosen since they do not superimpose with the diffuse ring of the liquid. Both pseudo-binary alloys, NiAl-Mo and NiAl-Cr, show small φ widths, concurrently for both phases. By contrast, alloys with intermediate Mo concentration exhibit higher φ widths. The preferred orientation at the SF does less deviate from the ideal preferred orientation for the alloys close to the pseudo-binary borders and becomes weaker for intermediate Mo concentrations.
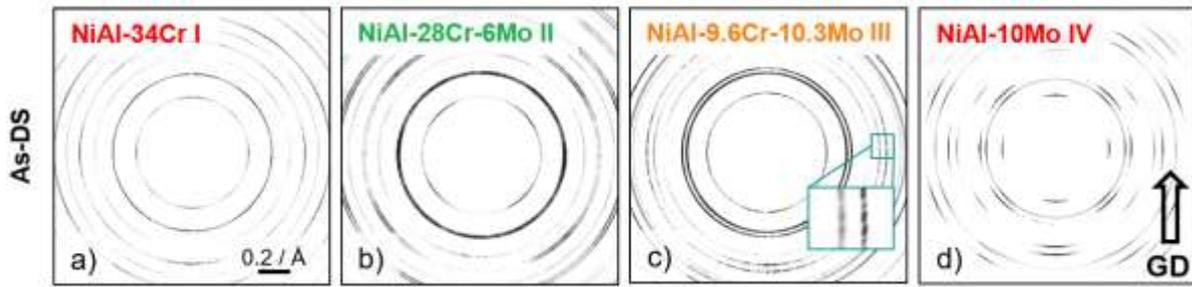
Fig. 6: Ex-situ synchrotron diffraction pattern in the as-DS condition: a) NiAl-34Cr, b) NiAl-28Cr-6Mo, c) NiAl-9.6Cr-10.3Mo and d) NiAl-10Mo. Diffracting sets of lattice planes are indicated in Fig. 4a. v was maintained at 60 mm/h for all alloys. The arrow indicates GD. GD is consistent for a) to d).

Fig. 6a to d show the pattern in the as-DS condition after cooling to room temperature. While the cooling does not change the patterns of NiAl-28Cr-6Mo and NiAl-10Mo, the intensity distribution for NiAl-9.6Cr-10.3Mo in Fig. 6c is nearly evenly distributed along the rings in comparison to sharp intensity maxima during nucleation of the eutectic colonies (Fig. 5c). This is due to the significantly larger solidification interval of alloys with intermediate Mo concentration [34], like for example 66 K for NiAl-9.6Cr-10.3Mo in comparison to 10 K and 3 K for NiAl-34Cr and NiAl-10Mo, respectively. The larger solidification interval leads to significant segregation, namely the colony nuclei solidify at higher Mo concentration than the regions solidifying at last [34].

3.3 Change of the preferred orientation

For NiAl-34Cr, further weak intensity maxima were developing in addition to the intensity maxima already present at the SF (Fig. 5a), indicating a change in preferred orientation during the solidification process (Fig. 6a). For the examination of the evolving preferred orientation, Fig. 7a shows the diffraction pattern of NiAl-34Cr solidified at v = 60 mm/h in detail. The lattice parameters of NiAl and Cr for this specific composition, a_{NiAl} and a_{Cr}, hardly differ from each other. Hence, the diffraction rings superimpose and the red-blue symbols in Fig. 7a mark the positions of the intensity maxima corresponding to both phases. The red symbols highlight the rings belonging exclusively to NiAl. The arrangement of the intensity maxima is caused by an alignment of both phases with ⟨001⟩ parallel to GD (about 23 multiples of the random distribution, m.r.d.). The arrows mark additional intensity maxima. The grey shaded {200} ring is further analyzed by means of rocking-curves in Fig. 7b. Additional rocking-curves of the {200} rings for various v between 18 mm/h and 180 mm/h are plotted as intensity

14

versus the azimuthal angle φ in Fig. 7b. Red, green and blue vertical lines mark the ideal peak positions of ⟨001⟩, ⟨110⟩ and ⟨111⟩ parallel to GD, respectively. Quantification of the preferred crystallographic orientations is presented in Fig. 7d. For v = 60 mm/h, it can be seen in Fig. 7b (grey shaded), that the arrows match well with the green vertical line, indicating an additional ⟨110⟩ fiber texture to the already established ⟨001⟩ parallel to GD (about 7 m.r.d.). For NiAl-34Cr, ⟨001⟩ preferred orientation was frequently reported in literature [4,17,33], while the ⟨111⟩ fiber component was only mentioned once in addition to a strong ⟨001⟩ fiber texture for as-DS NiAl-34Cr examined with v between 10 and 25 mm/h [5]. A change in positions of the intensity maxima is noticed for both, lower and higher v. Depending on v, the dominant preferred orientation varies. In contrast to Ref. [5], only ⟨111⟩ preferred orientation (about 8 m.r.d.) can be assigned without indications for any ⟨001⟩ parallel to GD for the lowest velocity consistent with the quantified information in Fig. 7d. This emphasizes the influence of the processing condition v. However, it also suggests that other process parameter such as temperature gradient, which also depend on the directional solidification device, have an influence on the evolving preferred orientation as well as on the growth velocity range in which the transitions in preferred orientation takes place.
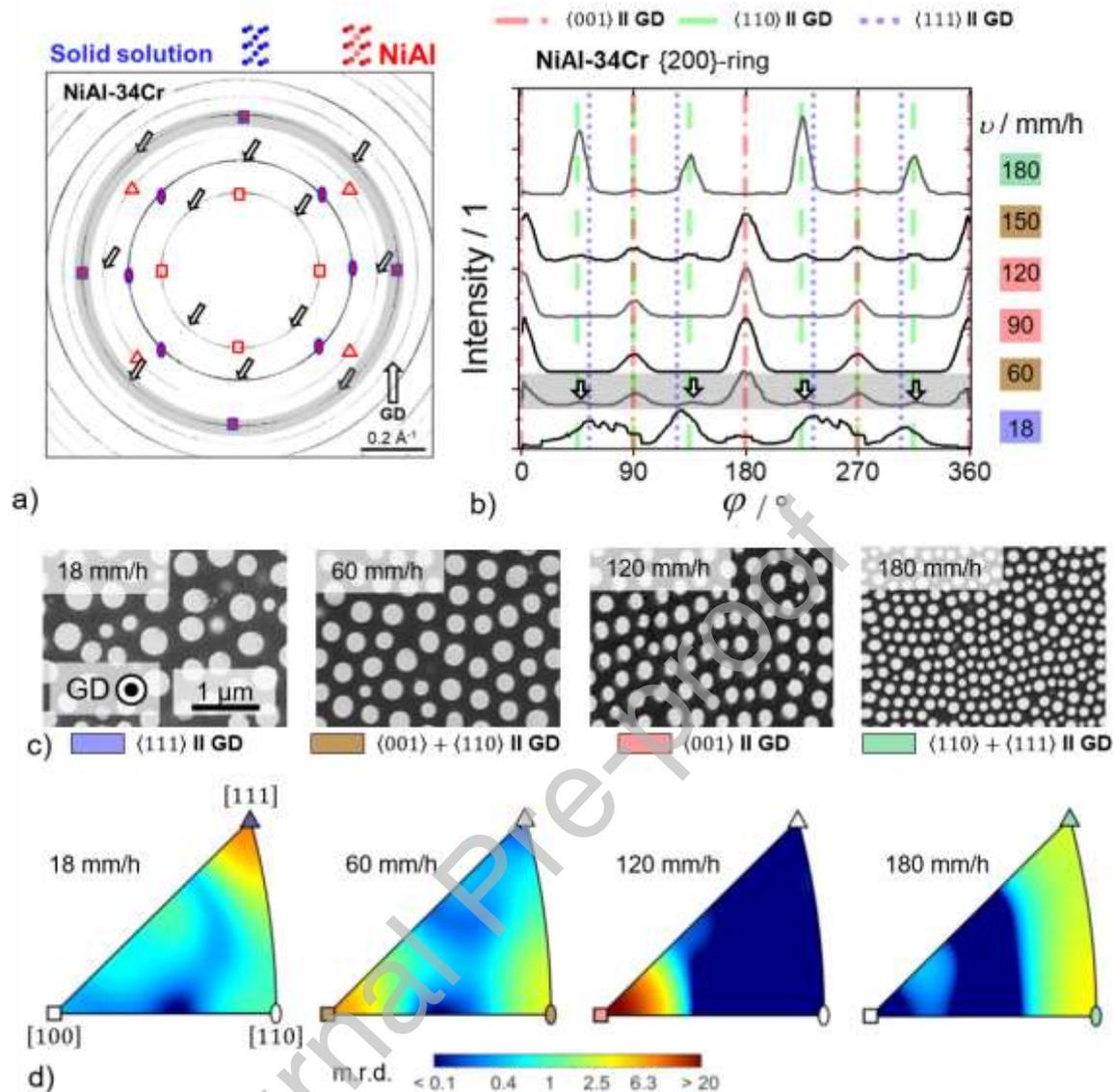
Fig. 7: a) Ex-situ synchrotron diffraction pattern of as-DS NiAl-34Cr at room temperature. The intensity maxima highlighted by red-blue symbols correspond to the rings of both phases, B2 NiAl and A2 Cr. Red symbols mark the diffraction rings only of the B2 superlattice of NiAl. The sets of diffracting lattice planes are marked by symbols: square for {100} and {200}, oval for {110} and triangle for {111}. b) Rocking curves of the {200} rings for several v obtained from ex-situ synchrotron diffraction patterns. c) Ex-situ SEM-BSE images of the cross-sections in as-DS condition perpendicular to GD. GD is consistent for all micrographs. d) Orientation distribution (consistent logarithmic color code in m.r.d.) within the inverse pole figure of GD obtained by refinement of ex-situ synchrotron diffraction patterns.

The addition of Mo to NiAl-34Cr reportedly changes the preferred orientation abruptly from ⟨001⟩ to ⟨111⟩ [17,33]. The change in preferred orientation was correlated to the lattice mismatch, the change in morphology as well as to the interfacial energy [17,33].

Since a changing preferred orientation was observed for the NiAl-34Cr alloy investigated in the present experiments, a change in interfacial energy due to addition of further elements can be excluded to account for the change in preferred orientation. The morphology investigated for four different v is shown in Fig. 7c. For all v, bright Cr is embedded in the dark NiAl matrix as fibers exclusively. Although the preferred orientation gradually changes from $\langle 111 \rangle$ to $\langle 001 \rangle$ towards mixed preferred orientations with increasing v, *no* change in morphology was observed. A change in preferred orientation does not lead to a change in morphology. In order to evaluate the impact of minor Mo addition, directionally solidified NiAl-33.4Cr-0.6Mo at 18 mm/h, 60 mm/h and 180 mm/h was investigated (not shown here). The lowest v leads to $\langle 111 \rangle$ parallel to GD and both higher growth velocities to $\langle 001 \rangle$ parallel to GD. Multiple preferred orientations were *not* detected.

Since strain energy reduction at coherent interfaces might drive the occurrence of preferred orientations, lattice mismatch during solidification and cooling was mapped. Therefore, the lattice parameters $a_{(Cr,Mo)}$ and a_{NiAl} of the individual phases (again, NiAl in red and $(Cr,Mo)_{ss}$ in blue color) were analyzed at the SF (semi-filled symbols) as well as in the as-DS condition at room temperature (open symbols) as a function of v. The results are plotted in Fig. 8a. v is linked to superheating and cooling conditions at the solidification front during the process, which might cause changes in the solubility of the elements close to the liquidus temperature. Thus, v has a strong impact on the lattice parameter of the solidifying crystals at the SF. The lattice mismatch δ at the SF and in the as-DS condition calculated by Eq. 1 are shown in Fig. 8b:

$$\delta = 2 \cdot \frac{a_{(Cr,Mo)} - a_{NiAl}}{a_{(Cr,Mo)} + a_{NiAl}} \qquad \text{Eq. 1}$$

δ is negative in the as-DS condition independent of v, which is in agreement with literature [4,17,33]. In contrast, δ at the SF is characterized by two zero transitions with increasing in v (from positive to negative and back to positive). Overlaying the results from the preferred orientation analysis in Fig. 7b as a color code in Fig. 8 clearly indicates that δ at the SF accounts for the evolving preferred orientation: positive δ values lead to $\langle 111 \rangle$ or mixed $\langle 110 \rangle + \langle 111 \rangle$ orientations parallel to GD while negative δ lead to dominant $\langle 001 \rangle$ parallel to GD. The same dependence of preferred orientation and δ was observed for directionally solidified NiAl-33.4Cr-0.6Mo solidified at 18, 60 and 180 mm/h. Equivalent to NiAl-34Cr, a zero transition (from positive to negative) of δ at the SF with increasing in v was found. Positive δ of 0.12 % at the SF was found for

17

NiAl-33.4Cr-0.6Mo at 18 mm/h. The positive δ cause growth of only $\langle 111 \rangle$ orientations parallel to GD, while for 60 and 180 mm/h with a negative δ of -0.05 % and -0.04 % respectively, $\langle 001 \rangle$ orientations parallel to GD prevail. The morphology of NiAl-33.4Cr-0.6Mo (not shown here) investigated for the three different v, also revealed no change in morphology with the change in preferred orientation.
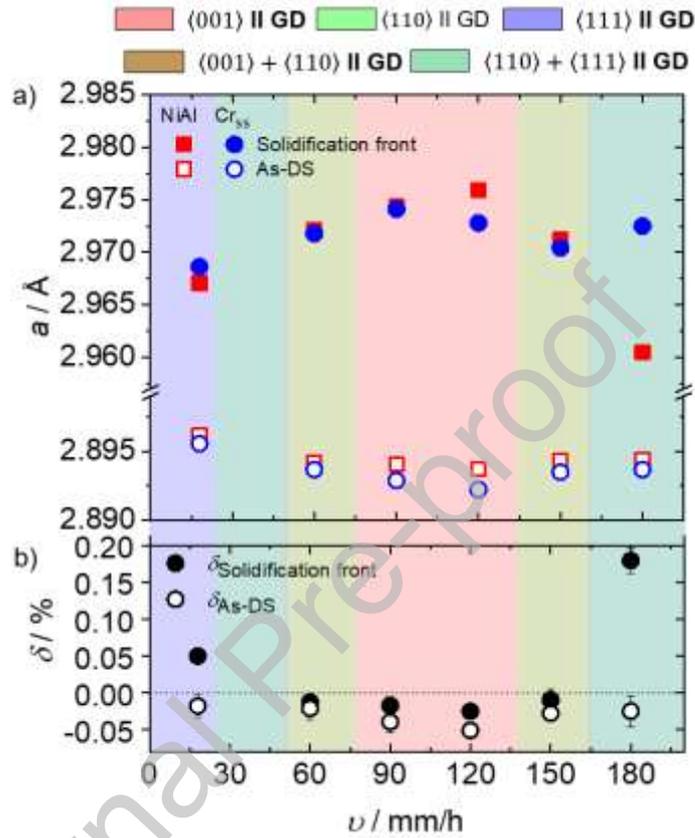

Fig. 8:   a) Lattice parameter a and b) Lattice mismatch δ of NiAl-34Cr at the SF (obtained from in-situ diffraction patterns) and in the as-DS condition at room temperature (from ex-situ diffraction patterns) as a function of the growth velocity v . Error bars are of symbol size. The color code is consistent with Fig. 7b. Mixed orientations result in yellow for $\langle 001 \rangle + \langle 110 \rangle$ and turquois for $\langle 110 \rangle + \langle 111 \rangle$.

Since the variation in preferred orientation in region **I** is coupled to the lattice mismatch at the solidification front, the lattice parameter and lattice mismatch evolution along the eutectic trough are discussed in detail in what follows.
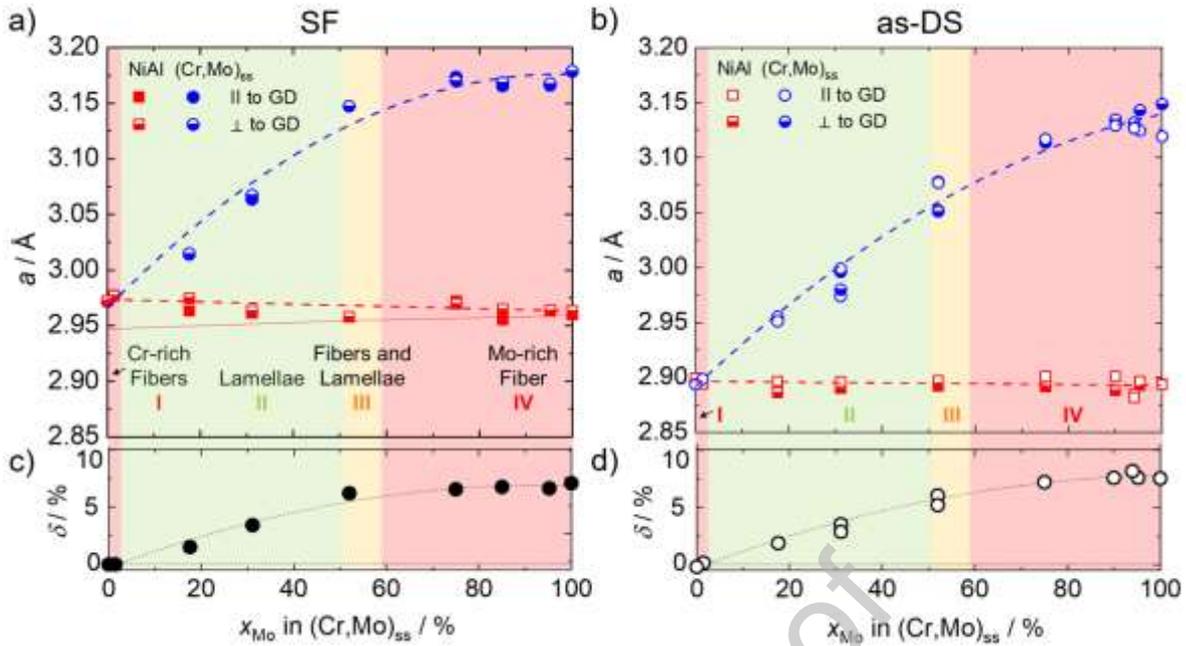
Fig. 9: Lattice parameters as a function of x_{Mo} in $(Cr,Mo)_{ss}$: a) at the SF (obtained from in-situ diffraction patterns) and b) in the as-DS condition (from ex-situ diffraction patterns) at $v = 60$ mm/h. Error bars are of symbol size. Red symbols refer to the lattice parameter of B2 NiAl while blue symbols represent those of A2 $(Cr,Mo)_{ss}$. The direction dependency is expressed by full and open symbols for lattice parameters parallel to GD and semi-filled for perpendicular to GD. δ parallel to GD as a function of x_{Mo} in $(Cr,Mo)_{ss}$: c) at the SF (deduced from a)) and d) in the as-DS condition (from b)).

The lattice parameters of both phases, NiAl and $(Cr,Mo)_{ss}$, and the lattice mismatch at the SF and in the as-DS condition are plotted as a function of x_{Mo} in $(Cr,Mo)_{ss}$ in Fig. 9a & b and Fig. 9c & d, respectively. Due to the different coefficients of thermal expansion (CTE) and the solubility of the elements close to the liquidus temperature, the lattice mismatch δ at the SF differs from that at room temperature [17]. So far, δ just below the liquidus temperature has only been estimated, since the CTE were experimentally determined only up to a temperature of 1000 °C and extrapolated towards the liquidus temperature [17,33,44]. Moreover, the influence of the solubility of other elements on δ close to the liquidus temperature was estimated by means of rapid quenching from a temperature of 50 K below the liquidus temperature [17]. The NiAl lattice parameter at the SF exhibits a slight decrease with increasing x_{Mo} in $(Cr,Mo)_{ss}$ (Fig. 9a). Estimation of a_{NiAl} of pure NiAl [45] at the respective liquidus temperatures along the eutectic trough predicts an increase in lattice parameter with increasing x_{Mo} in $(Cr,Mo)_{ss}$ (red solid line Fig. 9a). However, the solubility of Cr in NiAl close to liquidus temperature is significantly higher than of Mo (8 at.% Cr in NiAl and 0.1 % Mo in NiAl at the liquidus

19

temperature, see Fig. 1b), which explains the difference to the experimentally determined lattice parameter. The dissolved elements have only little influence on the CTE of NiAl [46], but they considerably change the lattice parameter at the solidification front due to the different solubility. Thus, it is not reasonable to determine δ or the lattice parameters by an extrapolation using the CTE [17,33]. The lattice parameter of the solid solution $a_{(Cr,Mo)}$ continuously increases with increasing x_{Mo} in $(Cr,Mo)_{ss}$ (Fig. 9a, blue symbols). The lattice parameter of $a_{Cr} = 2.972$ Å in NiAl-34Cr at the SF is similar to pure Cr with $a_{Cr} = 2.970$ Å close to the melting temperature of pure Cr [47–49]. The lattice parameter of $a_{Mo} = 3.179$ Å in NiAl-10Mo at the SF agrees well with the lattice parameter of pure Mo $a_{Mo} = 3.180$ Å at 1600 °C [50]. Moreover, no direction dependency with respect to GD was observed at the SF. Hence, the lattice parameters are isotropic at the SF and the phases are undistorted at the beginning of crystallization. The lattice parameter in the as-DS condition at room temperature is depicted in Fig. 9b. a_{NiAl} does not change with increasing x_{Mo} in $(Cr,Mo)_{ss}$, while $a_{(Cr,Mo)}$ increases with increasing x_{Mo}. Here, a direction dependency with respect to GD was found in the as-DS condition. $a_{(Cr,Mo)}$ (Fig. 9b, blue open symbols) was noted smaller parallel to GD than perpendicular to GD (Fig. 9b, blue semi-field symbols). The opposite behavior was found for a_{NiAl}, as it is greater parallel (Fig. 9b, red open symbols) than perpendicular to GD (Fig. 9b, red semi-field symbols). Both phases are distorted due to the different CTE in conjunction with the alignment of the phases. Refs. [51,52] suggest that the solid solution is under compression and the NiAl matrix under tension subsequent to cooling of NiAl-10Mo. As shown in the present study, this type of anisotropy occurs for alloys in the regions **II** to **IV**. Region **I** is less affected, since no significant direction dependence was found. The significant residual strains in the Mo-rich region **IV** can be attributed to the greater CTE difference between NiAl and the solid solution (with ΔCTE being $0.8 \cdot 10^{-5}$

and $0.3 \cdot 10^{-5}$ 1/K at room temperature between NiAl and Mo [44,50,53,54] as well as NiAl and Cr [2,47,49,55], respectively).

Due to directional solidification, the phase boundaries perpendicular to GD are greatly reduced and the phase boundaries along GD dominate. Thus, the following paragraph focuses on the lattice mismatch δ parallel to GD. Fig. 9c & d display δ calculated with Eq. 1 based on experimentally determined lattice parameters at the SF and in the as-DS condition. Since no direction-dependence between the lattice parameters was

determined at the SF, δ is also isotropic at the SF. As $a_{(Cr,Mo)}$ changes dramatically in contrast to a_{NiAl}, the Mo concentration is decisive for the lattice mismatch. δ is negative for NiAl-34Cr ($\delta = -0.31\%$), becomes zero around 2 % Mo in $(Cr,Mo)_{ss}$ and steadily increases to $\delta = 6.9$ % for NiAl-10Mo (Fig. 9c). In the as-DS condition a negative lattice mismatch of $\delta = -0.27$ % for NiAl-34Cr is seen and $\delta = 0$ % is found for the alloy with 1.8 % Mo in $(Cr,Mo)_{ss}$. This is in agreement with Ref. [17], but higher than in the as-cast condition reported in Ref. [34], which confirms that δ alters with the processing route. With further increase in x_{Mo} in $(Cr,Mo)_{ss}$, δ becomes greater and reaches $\delta = 7.9$ % in NiAl-10Mo. This is lower than reported in Refs. [15,56,57], which is most likely because the present study considered only δ parallel to GD.

In conclusion, the lattice mismatch δ at the SF is characterized by a sign change depending on v only for alloys in region **I**. This influences the growth of preferred orientations. Alloys with Mo concentrations higher than 2 % Mo in $(Cr,Mo)_{ss}$ exhibit only positive δ at the SF regardless of the solidification parameters. In region **II**, ⟨111⟩ retains parallel to GD and no further change in the preferred orientation occurs (see the respective synchrotron diffraction patterns at the SF in the Supplementary Material). With this in mind, still a fibrous morphology would be expected in region **II**, since the preferred orientation does not cause a change in morphology. However, the microstructural examination in Fig. 2c reveals a lamellar morphology, which is discussed in detail in the following section.

3.4 Orientation relationships in NiAl-(Cr,Mo) alloys

Due to the rotational symmetry by the in-situ directional solidification setup, the orientation relationship cannot be unequivocally determined (see for example the similar synchrotron diffraction patterns of fibrous NiAl-34Cr at 18 mm/h and lamellar NiAl-28Cr-6Mo at 60 mm/h in the Supplementary Material while different orientation relationships are present in the two alloys). Therefore, EBSD investigations were carried out for two alloys from region **II**, namely NiAl-31Cr-3Mo (Fig. 10a & c) and NiAl-28Cr-6Mo (Fig. 10b & d) revealing two different colony types. As indicated by the color code in the orientation maps in Fig. 10a & b for both alloys, ⟨111⟩ directions are parallel to GD. However, the obtained misorientation between the phases in NiAl-31Cr-3Mo was (59.9 ± 0.2)° about ⟨111⟩ (Type 2). This corresponds well to an orientation relationship described by a 60° rotation about a ⟨111⟩ axis as illustrated in the lower part of Fig. 10e

and is in agreement with the second possible orientation relationship reported for NiAl-9.6Cr-10.3Mo in Ref. [34]. A similar misorientation of $(59.8 \pm 0.2)°$ was found in NiAl-28Cr-6Mo for the upper right colony (Type 2) in Fig. 10b. These findings are in contradiction, however, with the reported cube-on-cube orientation relationship for these compositions [17,29,58–62]. For the lower-left colony, a misorientation of $(0.45 \pm 0.17)°$ was detected, which corresponds to the cube-on-cube orientation relationship (Fig. 10e, Type 1). Only Ref. [31] reported two orientation relationships in Hf- and Si-doped NiAl-31Cr-3Mo once. Several other authors continued to postulate the sole appearance of the cube-on-cube orientation relationship in the NiAl-Cr-Mo system [17,29,58–62]. The used technique was mostly transmission electron microscopy, which only provides local information of a few interfaces. Therefore, in this work SEM/EBSD was chosen for a more integral determination of the orientation relationships.
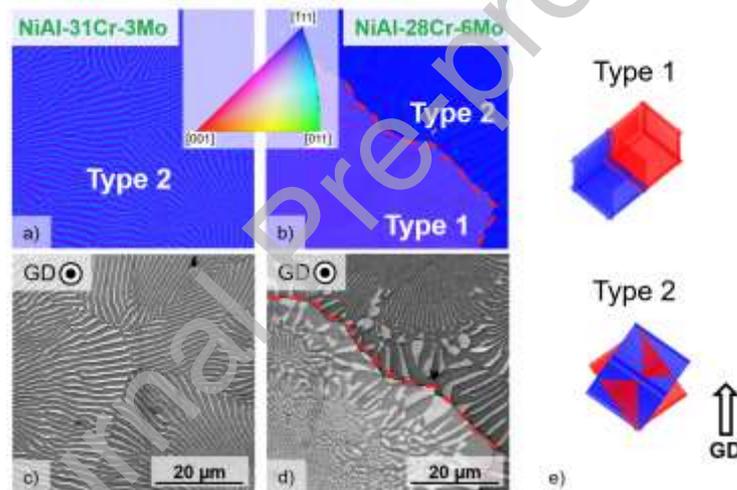

Fig. 10: Ex-situ orientation mapping according to the inverse pole figure of the normal surface to a cross-section of a) NiAl-31Cr-3Mo and b) NiAl-28Cr-6Mo obtained by EBSD. Image quality maps of c) NiAl-31Cr-3Mo and d) NiAl-28Cr-6Mo of the same field of view as in a and b, respectively. Red lines mark the interface between the two different colony types. e) Pictograms with {100} of the cube-on-cube (upper) and 60° rotation about ⟨111⟩ orientation relationship (lower) with A2 (Cr,Mo)$_{ss}$ in red and B2 NiAl in blue. ⟨111⟩ is parallel to GD for both colony types which corresponds to blue color in a) and b).

Refs. [34,63] suggested that the orientation relationship is decisive for the evolving morphology. This statement is confirmed by the present study. Only the second orientation relationship expressed by a 60° rotation about ⟨111⟩ was found in NiAl-31Cr-3Mo, which is the reason why the microstructure of NiAl-31Cr-3Mo (Fig. 10c)

consists only of $(Cr,Mo)_{ss}$ lamellae within the NiAl matrix. In NiAl-28Cr-6Mo, two different types of colonies were observed (Fig. 10d). Equivalent to NiAl-31Cr-3Mo, a lamellar morphology was found for the Type 2 colony (Fig. 10d), while the Type 1 colony possesses fibrous morphology and a cube-on-cube orientation relationship (Fig. 10d). To conclude, the orientation relationship determines the morphology.
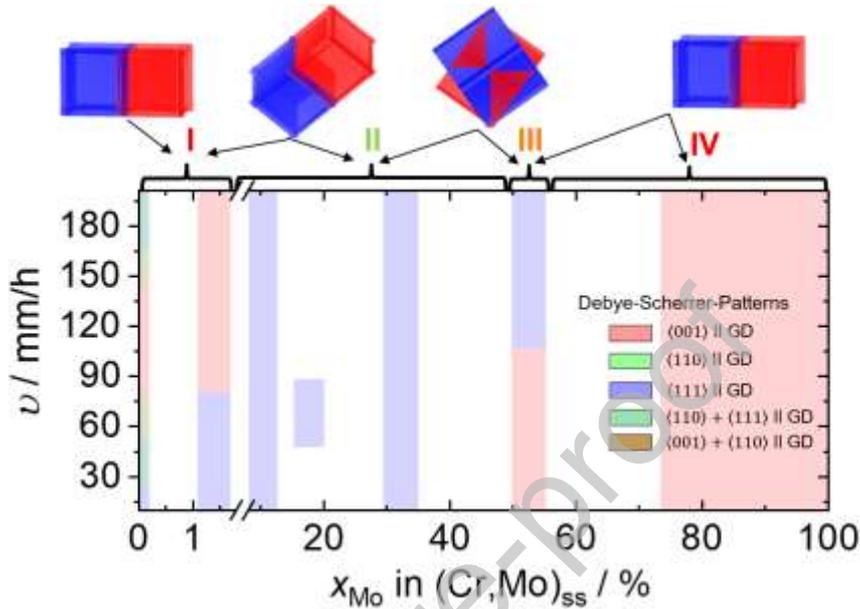

Fig. 11: Summary on the appearance of preferred orientations as a function of x_{Mo} in $(Cr,Mo)_{ss}$ and growth velocity v. Colored regions correspond to preferred orientations derived from the synchrotron diffraction patterns (see Figs. 6 & 7). The pictograms summarize the proven orientation relationships between A2 $(Cr,Mo)_{ss}$ in red and B2 NiAl in blue (see Fig. 10). **I** to **IV** represent the adapted classification based on the morphology.

Fig. 11 summarizes the EBSD results combined with the preferred orientations obtained by synchrotron diffraction patterns at various v and as a function of x_{Mo} in $(Cr,Mo)_{ss}$. The adapted morphologies are also included. In region **I**, the cube-on-cube orientation relationship with different crystallographic preferred orientations and fibrous morphology were exclusively observed.

The dominant orientation relationship changes to a 60° rotation about ⟨111⟩ in region **II** and mainly lamellar morphology forms. Only occasionally, colonies with the cube-on-cube orientation relationship and fibrous morphology were found. The preferred orientation was exclusively ⟨111⟩ parallel to GD. Since no distinct habit plane was observed for the 60° orientation relationship (see Fig. 10), these eutectic colonies need to grow coupled in the common direction of both phases, namely the ⟨111⟩, equivalent to the preferred orientation. The fact that one or two orientation relationships can be present in the microstructure, suggests that during directional solidification, the growth

23

of the favorable orientation and the elimination of the other orientations are competing mechanisms [64].

In region **III**, both orientation relationships and morphologies as well as both preferred orientations with ⟨001⟩ and ⟨111⟩ parallel to GD are present depending on v.

Regardless of the solidification parameters, a cube-on-cube orientation relationship, a⟨001⟩ preferred orientation and a fibrous morphology was exclusively observed in region **IV**. The tendency to fiber formation is most likely due to the poor lattice matching (δ > 6 %) and the fact that in contrast to the lamellae fibers require only a periodic coincidences in atomic rows along GD [65].

4. Conclusions

Following conclusions can be drawn on directional solidification of eutectic NiAl-(Cr,Mo) alloys from this study:

- The classification of the eutectic trough into four regions (fibers, **I**; lamellae, **II**; lamellae + fibers, **III**; fibers, **IV**), according to different morphologies in the as-cast condition proposed in Ref. [34] can be extended to considering orientation relationship and formation of preferred orientation.

- The following preferred orientations are observed: ⟨001⟩ parallel to GD was observed in regions **I**, **III** and **IV**, while dominant ⟨111⟩ parallel to GD was found in region **II**. Preferred orientation is present already during nucleation. Larger deviations from the ideal orientation sites occur for intermediate Mo contents due to extended solidification intervals.

- For alloys in region **I** (incl. NiAl-Cr), the sign of the lattice mismatch δ at the SF determines the evolving preferred orientations. δ clearly depends on dissolved Cr and Mo due to changing lattice parameters. The impact of growth rate v on δ arises from altered superheating of the liquid and cooling rate, and hence dissolved amount of Cr or Mo. δ at room temperature is negative for all these alloys in the as-DS state at room temperature due to superimposed thermal expansion; it should not be evaluated for assessment of the preferred orientation change. For alloys beyond region **I**, large positive δ irrespective of the processing conditions are present and increase with increasing Mo concentration in $(Cr,Mo)_{ss}$.

- No changes in morphology were observed in region **I** even when changes in preferred orientation or multiple ideal sites of preferred orientaitons were present This is indicating an independence of morphology and preferred orientation from another. The simultaneous appearance of colonies with two different orientation relationships (60° rotation about ⟨111⟩ vs. cube-on-cube) and of different morphologies (lamellar and fibrous, respectively) in region **II** reveals the morphology control by the orientation relationship. Since no distinct habit plane was observed for the 60° orientation relationship, these eutectic colonies can only grow coupled in the common direction of both phases, e.g. ⟨111⟩, equivalent to the preferred orientation. Hence, preferred orientation stems from the interplay of orientation relationship and morphology in these cases.

Prime novelty statement

We confirm that this manuscript has not been published previously by any of the authors and is not under consideration for publication in another journal.

Declaration of competing interest

The authors declare that they have no known competing financial interests or personal relationships that could have appeared to influence the work reported in this paper.

Acknowledgments

References

[1]   D.B. Miracle, Overview No. 104 The physical and mechanical properties of NiAl, Acta Metallurgica et Materialia 41 (1993) 649–684. https://doi.org/10.1016/0956-7151(93)90001-9.

[2]   R.D. Noebe, R.R. Bowman, M.V. Nathal, Physical and mechanical properties of the B2 compound NiAl, International Materials Reviews 38 (1993) 193–232. https://doi.org/10.1179/imr.1993.38.4.193.

[3]   F. Ebrahimi, S. Shrivastava, Brittle-to-ductile transition in NiAl single crystal, Acta Materialia 46 (1998) 1493–1502. https://doi.org/10.1016/S1359-6454(97)00370-4.

[4]   H.E. Cline, J.L. Walter, E. Lifshin, R.R. Russell, Structures, faults, and the rod-plate transition in eutectics, Metallurgical Transactions 2 (1971) 189–194. https://doi.org/10.1007/BF02662656.

[5]   G. Frommeyer, R. Rablbauer, H.J. Schäfer, Elastic properties of B2-ordered NiAl and NiAl–X (Cr, Mo, W) alloys, Intermetallics 18 (2010) 299–305. https://doi.org/10.1016/j.intermet.2009.07.026.

[6]   R. Rablbauer, G. Frommeyer, F. Stein, Determination of the constitution of the quasi–binary eutectic NiAl–Re system by DTA and microstructural investigations, Materials Science and Engineering: A 343 (2003) 301–307. https://doi.org/10.1016/S0921-5093(02)00388-X.

[7] S. M. Joslin, X. F. Chen, B. F. Oliver, R. D. Noebe, Fracture behavior of directionally solidified NiAl-Mo and NiAl-V eutectics, Materials Science and Engineering: A 196 (1995) 9–18. https://doi.org/10.1016/0921-5093(94)09683-X.

[8] D. R. Johnson, X. F. Chen, B. F. Oliver, R. D. Noebe, J. D. Whittenberger, Processing and mechanical properties of in-situ composites from the NiAl-Cr and the NiAl-(Cr,Mo) eutectic systems, Intermetallics 3 (1995) 99–113. https://doi.org/10.1016/0966-9795(95)92674-O.

[9] M. Dudová, K. Kuchařová, T. Barták, H. Bei, E. P. George, C. Somsen, A. Dlouhý, Creep in directionally solidified NiAl–Mo eutectics, Scripta Materialia 65 (2011) 699–702. https://doi.org/10.1016/j.scriptamat.2011.07.019.

[10] C. Seemüller, M. Heilmaier, T. Haenschke, H. Bei, A. Dlouhy, E. P. George, Influence of fiber alignment on creep in directionally solidified NiAl–10Mo in-situ composites, Intermetallics 35 (2013) 110–115. https://doi.org/10.1016/j.intermet.2012.12.007.

[11] T. Haenschke, A. Gali, M. Heilmaier, M. Krüger, H. Bei, E.P. George, Synthesis and characterization of lamellar and fibre-reinforced NiAl-Mo and NiAl-Cr, Journal of Physics: Concerence Series 240 (2010) 12063. https://doi.org/10.1088/1742-6596/240/1/012063.

[12] A. Misra, R. Gibala, Plasticity in multiphase intermetallics, Intermetallics 8 (2000) 1025–1034. https://doi.org/10.1016/S0966-9795(00)00079-0.

[13] J. F. Zhang, J. Shen, Z. Shang, Z. R. Feng, L. Wang, H. Fu, Microstructure and room temperature fracture toughness of directionally solidified NiAl–Mo eutectic in situ composites, Intermetallics 21 (2012) 18–25. https://doi.org/10.1016/j.intermet.2011.10.002.

[14] S. Milenkovic, R. Caram, Mechanical Properties and Fracture Behavior of Directionally Solidified NiAl-V Eutectic Composites, Metallurgical and Materials Transactions A 46 (2015) 557–565. https://doi.org/10.1007/s11661-014-2427-6.

[15] H. Bei, E. P. George, Microstructures and mechanical properties of a directionally solidified NiAl–Mo eutectic alloy, Acta Materialia 53 (2005) 69–77. https://doi.org/10.1016/j.actamat.2004.09.003.

[16] J. Albiez, I. Sprenger, C. Seemüller, D. Weygand, M. Heilmaier, T. Böhlke, Physically motivated model for creep of directionally solidified eutectics evaluated for the intermetallic NiAl–9Mo, Acta Materialia 110 (2016) 377–385. https://doi.org/10.1016/j.actamat.2016.02.024.

[17] H. E. Cline, J. L. Walter, The Effect of Alloy Additions on the Rod-Plate Transition in the Eutectic NiAl-Cr, Metallurgical Transactions 1 (1970) 2907–2917. https://doi.org/10.1007/bf03037830.

[18] M. Kellner, J. Hötzer, E. Schoof, B. Nestler, Phase-field study of eutectic colony formation in NiAl-34Cr, Acta Materialia 182 (2020) 267–277. https://doi.org/10.1016/j.actamat.2019.10.028.

27

[19] A. Kumar, C. Ensslen, A. Krüger, M. Klimenkov, O. Kraft, R. Schwaiger, Micromechanical study on the deformation behavior of directionally solidified NiAl–Cr eutectic composites, Journal of Materials Research 32 (2017) 2127–2134. https://doi.org/10.1557/jmr.2017.23.

[20] J. D. Whittenberger, S. V. Raj, I. E. Locci, J. A. Salem, Effect of growth rate on elevated temperature plastic flow and room temperature fracture toughness of directionally solidified NiAl-31Cr-3Mo, Intermetallics 7 (1999) 1159–1168. https://doi.org/10.1016/S0966-9795(99)00023-0.

[21] J. D. Whittenberger, S. V. Raj, I. E. Locci, J. A. Salem, Effects of minor alloying additions on the microstructure, toughness and creep strength of directionall solidified NiAl-31Cr-3Mo, Structural Intermetallics (2001) 775–784.

[22] J. D. Whittenberger, S. V. Raj, I. E. Locci, J. A. Salem, Elevated Temperature Strength and Room-Temperature Toughness of Directionally Solidified Ni-33Al-33Cr-1Mo, Metallurgical and Materials Transactions A 33A (2002) 1385–1397. https://doi.org/10.1007/s11661-002-0063-z.

[23] X.F. Chen, D.R. Johnson, R.D. Noebe, B. F. Oliver, Deformation and fracture of a directionally solidified NiAl–28Cr–6Mo eutectic alloy, Journal of Materials Research 10 (1995) 1159–1170. https://doi.org/10.1557/JMR.1995.1159.

[24] J. Peng, P. Franke, H.J. Seifert, Experimental Investigation and CALPHAD Assessment of the Eutectic Trough in the System NiAl-Cr-Mo, Journal of Phase Equilibria and Diffusion 37 (2016) 592–600. https://doi.org/10.1007/s11669-016-0490-y.

[25] J. Peng, X. Fang, Z. Qu, J. Wang, Isothermal oxidation behavior of NiAl and NiAl-(Cr,Mo) eutectic alloys, Corrosion Science 151 (2019) 27–34. https://doi.org/10.1016/j.corsci.2019.02.011.

[26] G. Geramifard, C. Gombola, P. Franke, H.J. Seifert, Oxidation behaviour of NiAl intermetallics with embedded Cr and Mo, Corrosion Science 177 (2020) 108956. https://doi.org/10.1016/j.corsci.2020.108956.

[27] S. Gabel, S. Giese, B. Merle, I. Sprenger, M. Heilmaier, S. Neumeier, E. Bitzek, M. Göken, Microcantilever Fracture Tests on Eutectic NiAl–Cr(Mo) In Situ Composites, Advanced Engineering Materials (2021) 2001464. https://doi.org/10.1002/adem.202001464.

[28] A. Förner, S. Giese, C. Arnold, P. Felfer, C. Körner, S. Neumeier, M. Göken, Nanoscaled eutectic NiAl-(Cr,Mo) composites with exceptional mechanical properties processed by electron beam melting, Scientific reports 10 (2020) 15153. https://doi.org/10.1038/s41598-020-72093-5.

[29] J.T. Guo, C.Y. Cui, Y.X. Chen, D.X. Li, H.Q. Ye, Microstructure, interface and mechanical property of the DS NiAl/Cr(Mo,Hf) composite, Intermetallics 9 (2001) 287–297. https://doi.org/10.1016/S0966-9795(01)00009-7.

[30] Y.X. Chen, C.Y. Cui, J.T. Guo, D.X. Li, Microstructure investigation of NiAl–Cr(Mo) interface in a directionally solidified NiAl–Cr(Mo) eutectic alloyed with refractory metal, Materials Science and Engineering: A 373 (2004) 279–285. https://doi.org/10.1016/j.msea.2004.01.026.

[31] A. Misra, R. Gibala, R. D. Noebe, Optimization of toughness and strength in multiphase intermetallics, Intermetallics 9 (2001) 971–978. https://doi.org/10.1016/S0966-9795(01)00098-X.

[32] R. I. Barabash, W. Liu, J. Z. Tischler, H. Bei, J. D. Budai, Phase-specific elastic/plastic interface interactions in layered NiAl–Cr(Mo) structures, Acta Materialia 60 (2012) 3279–3286. https://doi.org/10.1016/j.actamat.2012.02.052.

[33] H.E. Cline, J.L. Walter, E.F. Koch, L.M. Osika, The variation of interface dislocation networks with lattice mismatch in eutectic alloys, Acta Metallurgica 19 (1971) 405–414. https://doi.org/10.1016/0001-6160(71)90163-5.

[34] C. Gombola, A. Kauffmann, G. Geramifard, M. Blankenburg, M. Heilmaier, Microstructural Investigations of Novel High Temperature Alloys Based on NiAl-(Cr,Mo), Metals 10 (2020) 961. https://doi.org/10.3390/met10070961.

[35] J. Peng, Experimental investigation and thermodynamic modeling of the Al-Cr-Mo-Ni system and its sub-systems (Dissertation), Karlsruher Institut für Technologie, Karlsruhe, 2016.

[36] C. Gombola, G. Hasemann, A. Kauffmann, I. Sprenger, S. Laube, A. Schmitt, F. Gang, V. Bolbut, M. Oehring, M. Blankenburg, N. Schell, P. Staron, F. Pyczak, M. Krüger, M. Heilmaier, A zone melting device for the in situ observation of directional solidification using high-energy synchrotron x rays, Review of scientific instruments 91 (2020) 93901. https://doi.org/10.1063/5.0019020.

[37] A. P. Hammersley, FIT2D: An Introduction and Overview, ESFR Internal Report, ESRF97HA02T, Grenoble, 1997.

[38] A. P. Hammersley, FIT2D V9.129 Reference Manual V3.1998, 1, ESRF Internal Report, ESRF98HA01T, Grenoble, 1998.

[39] L. Lutterotti, R. Vasin, H.-R. Wenk, Rietveld texture analysis from synchrotron diffraction images. I. Calibration and basic analysis, Powder Diffraction 29 (2014) 76–84. https://doi.org/10.1017/S0885715613001346.

[40] Maud: Material Analysis Using Diffraction (2022), Retrieved from http://maud.radiographema.eu, 02.02.2022.

[41] J.B. Nelson, D.P. Riley, An experimental investigation of extrapolation methods in the derivation of accurate unit-cell dimensions of crystals, Proceedings of the Physical Society 57 (1945) 160–177. https://doi.org/10.1088/0959-5309/57/3/302.

[42] O. Engler, V. Randle (Eds.), Texture analysis: Macrotexture, microtexture and orientation mapping, CRC Press, Boca Raton, 2010.

[43] K.-D. Liss, A. Bartels, A. Schreyer, H. Clemens, High-energy X-rays: a tool for advanced bulk investigations in materials science and physics, Textures and Microstructures 35 (2003) 219–252. https://doi.org/10.1080/07303300310001634952.

[44] H. Bei, E.P. George, D.W. Brown, G.M. Pharr, H. Choo, W.D. Porter, M.A.M. Bourke, Thermal-expansion behavior of a directionally solidified NiAl–Mo composite investigated by neutron diffraction and dilatometry, Acta Materialia 97 (2005) 123503. https://doi.org/10.1063/1.1929853.

[45] T. Hughes, E.P. Lautenschlager, J.B. Cohen, J.O. Brittain, X‑ray diffraction investigation of β'-NiAl alloys, Journal of Applied Physics 42 (1971) 3705–3716. https://doi.org/10.1063/1.1659674.

[46] R. Darolia, W. S. Walston, M. V. Nathal, NiAl Alloys for Turbines Airfoils, Superalloys (1996) 561–570.

[47] N.A. Dubrovinskaia, L.S. Dubrovinsky, S.K. Saxena, B. Sundman, Thermal expansion of Chromium (Cr) to melting temperature, Calphad 21 (1997) 497–508. https://doi.org/10.1016/S0364-5916(98)00007-8.

[48] R.G. Ross, W. Hume-Rothery, High temperature X-ray metallography, Journal of the Less Common Metals 5 (1963) 258–270. https://doi.org/10.1016/0022-5088(63)90031-6.

[49] G.K. White, C. Andrikidis, Thermal expansion of chromium at high temperature, Physical Review B 53 (1996) 8145–8147. https://doi.org/10.1103/PhysRevB.53.8145.

[50] J.W. Edwards, R. Speiser, H.L. Johnston, High Temperature Structure and Thermal Expansion of Some Metals as Determined by X‑Ray Diffraction Data. I. Platinum, Tantalum, Niobium, and Molybdenum, Journal of Applied Physics 22 (1951) 424–428. https://doi.org/10.1063/1.1699977.

[51] J. Kwon, M. L. Bowers, M. C. Brandes, V. McCreary, I. M. Robertson, P. Sudaharshan Phani, H. Bei, Y. F. Gao, G. M. Pharr, E. P. George, M. J. Mills, Characterization of dislocation structures and deformation mechanisms in as-grown and deformed directionally solidified NiAl–Mo composites, Acta Materialia 89 (2015) 315–326. https://doi.org/10.1016/j.actamat.2015.01.059.

[52] H. Bei, E. P. George, G. M. Pharr, Small-scale mechanical behavior of intermetallics and their composites, Materials Science and Engineering: A 483-484 (2008) 218–222. https://doi.org/10.1016/j.msea.2006.12.185.

[53] A. Misra, Z. L. Wu, M. T. Kush, R. Gibala, Deformation and fracture behaviour of directionally solidified NiAl-Mo and NiAl-Mo(Re) eutectic composites, Philosophical Magazine A 78 (1998) 533–550. https://doi.org/10.1080/01418619808241921.

[54] A. Misra, Z. L. Wu, M. T. Kush, R. Gibala, Microstructures and mechanical properties of directionally solidified NiAl–Mo and NiAl–Mo(Re) eutectic alloys, Materials Science and Engineering: A 239-240 (1997) 75–87. https://doi.org/10.1016/S0921-5093(97)00563-7.

[55] J.P. Moore, R.K. Williams, R.S. Graves, Thermal conductivity, electrical resistivity, and Seebeck coefficient of high‐purity chromium from 280 to 1000 K, Philosophical Magazine 48 (1977) 610–617. https://doi.org/10.1063/1.323697.

[56] L. Hu, G. Zhang, W. Hu, G. Gottstein, S. Bogner, A. Bührig-Polaczek, Tensile creep of directionally solidified NiAl–9Mo in situ composites, Acta Materialia 61 (2013) 7155–7165. https://doi.org/10.1016/j.actamat.2013.08.017.

[57] L. Hu, W. Hu, G. Gottstein, S. Bogner, S. Hollad, A. Bührig-Polaczek, Investigation into microstructure and mechanical properties of NiAl-Mo composites produced by directional solidification, Materials Science and Engineering: A 539 (2012) 211–222. https://doi.org/10.1016/j.msea.2012.01.083.

[58] D.R. Johnson, X.F. Chen, B.F. Oliver, R.D. Noebe, J.D. Whittenberger, Directional solidification and mechanical properties of NiAl-NiAlTa alloys, Intermetallics 3 (1995) 141–152. https://doi.org/10.1016/0966-9795(95)92679-T.

[59] Y.X. Chen, C.Y. Cui, L.L. He, J.T. Guo, D.X. Li, Theoretical and experimental studies of the dislocation structure at the NiAl–Cr(Mo) interfaces, Materials Letters 44 (2000) 186–191. https://doi.org/10.1016/S0167-577X(00)00024-0.

[60] Z. Shang, J. Shen, G. Liu, Y.H. Xu, Microstructure evolution of directionally solidified NiAl–28Cr–6Mo eutectic alloy under different withdrawal rates, Materials Science and Technology 34 (2018) 1839–1846. https://doi.org/10.1080/02670836.2018.1484842.

[61] C.Y. Cui, J.T. Guo, Y.H. Qi, H.Q. Ye, Deformation behavior and microstructure of DS NiAl/Cr(Mo) alloy containing Hf, Intermetallics 10 (2002) 1001–1009. https://doi.org/10.1016/S0966-9795(02)00124-3.

[62] J.-M. Yang, S. M. Jeng, K. Bain, R. A. Amato, Microstructure and mechanical behavior of in-situ directional solidified NiAl/Cr(Mo) eutectic composite, Acta Materialia 45 (1997) 295–308. https://doi.org/10.1016/S1359-6454(96)00124-3.

[63] S. Milenkovic, R. Caram, Growth morphology of the NiAl–V in situ composites, Journal of Materials Processing Technology 143-144 (2003) 629–635. https://doi.org/10.1016/S0924-0136(03)00449-7.

[64] S. Suwas, R. K. Ray (Eds.), Crystallographic Texture of Materials, Springer London, London, 2014.

[65] B.P. Bewlay, J.A. Sutliff, M.R. Jackson, K.M. Chang, Processing, Microstructures, and Properties of Cr-Cr3Si, Nb-Nb3Si, and V-V3Si Eutectics, Materials and Manufacturing Processes 9 (1994) 89–109. https://doi.org/10.1080/10426919408934887.